Structures of the Bacterial Ribosome at 3.5 Å Resolution

Barbara S. Schuwirth,[1,4]* Maria A. Borovinskaya,[3]*
Cathy W. Hau,[2] Wen Zhang,[1] Antón Vila-Sanjurjo,[3]
James M. Holton,[3] Jamie H. Doudna Cate[1,2,3]†

We describe two structures of the intact bacterial ribosome from *Escherichia coli* determined to a resolution of 3.5 angstroms by x-ray crystallography. These structures provide a detailed view of the interface between the small and large ribosomal subunits and the conformation of the peptidyl transferase center in the context of the intact ribosome. Differences between the two ribosomes reveal a high degree of flexibility between the head and the rest of the small subunit. Swiveling of the head of the small subunit observed in the present structures, coupled to the ratchet-like motion of the two subunits observed previously, suggests a mechanism for the final movements of messenger RNA (mRNA) and transfer RNAs (tRNAs) during translocation.

Protein biosynthesis occurs on the ribosome in all forms of life. Ribosomes in bacteria are 21-nm particles composed of a small (30*S*) and a large (50*S*) subunit that associate to form the intact 70*S* ribosome (*1*). In contrast to most cellular machines, the ribosome contains a functional core of RNA that is enhanced by ribosomal proteins and accessory factors. All ribosomal functions rely in large measure—in some cases entirely—on ribosomal RNA (rRNA). In particular, rRNA is responsible for catalyzing peptide bond formation (*2*, *3*) and contributes to mRNA decoding and to mRNA and tRNA translocation after peptide bond formation (*4*–*6*).

Atomic-resolution structures of the 30*S* and 50*S* ribosomal subunits have provided insight into the mechanism of protein synthesis (*1*, *6*, *7*). However, protein synthesis occurs only in the context of the intact ribosome. Initiation of translation generally begins with mRNA start codon recognition and initiator tRNA binding to the small subunit. Subsequently, the large subunit associates with the small-subunit complex, and the elongation cycle begins (*1*). During the elongation cycle, the ribosomal subunits maintain a delicate balance of stable interactions with a large degree of flexibility. The structure of the translating ribosome has been modeled by comparing atomic-resolution structures of the 30*S* and 50*S* subunits (*8*–*11*) with low-resolution x-ray crystal structural models and several cryo–electron microscopic (cryo-EM) reconstructions of the *E. coli* 70*S* ribosome and of the yeast and mammalian 80*S* ribosome (*12*–*29*). Although the low-resolution structures reveal many of the large-scale motions in the ribosome that occur during the elongation cycle, the underlying molecular mechanisms that control these motions remain unknown.

We now describe two structures of the intact 70*S* ribosome from *E. coli* at a resolution of 3.5 Å, based on crystals that contain two independent copies of the ribosome per asymmetric unit. Intriguingly, the two ribosomes in the crystal adopt strikingly different conformations that may relate to the trigger of mRNA and tRNA movements on the small subunit during translocation (*30*, *31*). The structures also reveal a high degree of solvation at the subunit interface that may facilitate intersubunit movement (*16*). Finally, relative to isolated large subunits, the structures of the intact ribosome exhibit differences in the peptidyl transferase center that may reflect the dynamics necessary for rapid peptide bond formation.

Structure determination. *E. coli* 70*S* ribosomes, purified as described (*14*) and depleted of ribosomal protein S1 (*32*), formed crystals that contained two unique copies of the ribosome and diffracted x-rays to beyond 3.5 Å resolution (table S1) (*33*). Structure factor phases were initially obtained by molecular replacement using a 9 Å resolution model of the 70*S* ribosome derived from atomic-resolution structures of the 30*S* and 50*S* subunits (*14*). The resulting model for two ribosomes was then refined against 3.5 Å structure factor amplitudes by iterative rounds of torsional dynamics and manual rebuilding (table S1) (*33*). Differences in the structures of the two ribosomes limited the use of noncrystallographic restraints in the refinement to domains within the small and large ribosomal subunits (table S2) (*33*).

The present model consists of two ribosomes in which the rRNAs (16*S* rRNA, helices h1 to h45, in the small subunit; 23*S* rRNA, helices H1 to H101, and 5*S* rRNA in the large subunit) and ribosomal proteins (S2 to S21 and L2 to L36 in the small and large subunits, respectively) are modeled with *E. coli* sequence (*34*, *35*). Because refinement of the large-subunit proteins is ongoing, the results presented here include only those large-subunit proteins for which the modeling is nearly complete. At 3.5 Å resolution, the RNA backbone is visible and bases can be distinguished at the level of purines and pyrimidines in many regions of the structure. Ribose puckers have been modeled on the basis of stereochemical constraints on the allowed torsional angles in nucleotides and their fit to electron density maps. The proteins are generally resolved at the level of the backbone, and protein side chains are evident in well-ordered regions. In addition, hydrated magnesium ions appear clearly in most parts of the electron density map. The model contains more than 170 Mg^{2+} ions per ribosome.

Figure 1 shows the overall structure of one of the ribosomes in the "standard" view (Fig. 1A; 30*S* subunit in front, 50*S* subunit to the rear) and in a "top" view (Fig. 1B). Recognizable features of the small subunit include the head, body, shoulder, platform, and spur. On the large subunit, the main features include the L1 arm, consisting of protein L1 and its 23*S* rRNA binding site; the central protuberance (CP); the A-site finger (ASF) RNA helix; and the region near proteins L7/L12, which includes the L11 arm, consisting of protein L11 and its 23*S* rRNA binding site. Nearly all of the rRNA and proteins are visible in the electron density. The structural elements that are not fully modeled because of disorder include regions that are known to be highly mobile within the ribosome (*21*, *27*, *36*): most of the L1 arm (L1 in Fig. 1), proteins L10, L7/L12, the end of the ASF, the free end of the L11 arm, and the N and C termini of some of the ribosomal proteins.

Rotation of the 30*S* subunit head and implications for tRNA movement. The two ribosomes in the crystallographic asymmetric unit (termed ribosomes I and II) adopt different conformations primarily as a result of rigid-body motions of domains within the subunits. The most striking difference is that the head of the small subunit has swiveled as a rigid body around the neck region by 6° in the direction of the exit tRNA binding site (E site) in ribosome II when compared to ribosome I

---

[1]Department of Chemistry, [2]Department of Molecular and Cell Biology, University of California, Berkeley, CA 94720, USA. [3]Physical Biosciences Division, Lawrence Berkeley National Laboratory, Berkeley, CA 94720, USA. [4]Institute of Chemistry-Crystallography, Free University of Berlin, 14195 Berlin, Germany.

*These authors contributed equally to this work.
†To whom correspondence should be addressed. E-mail: jcate@lbl.gov

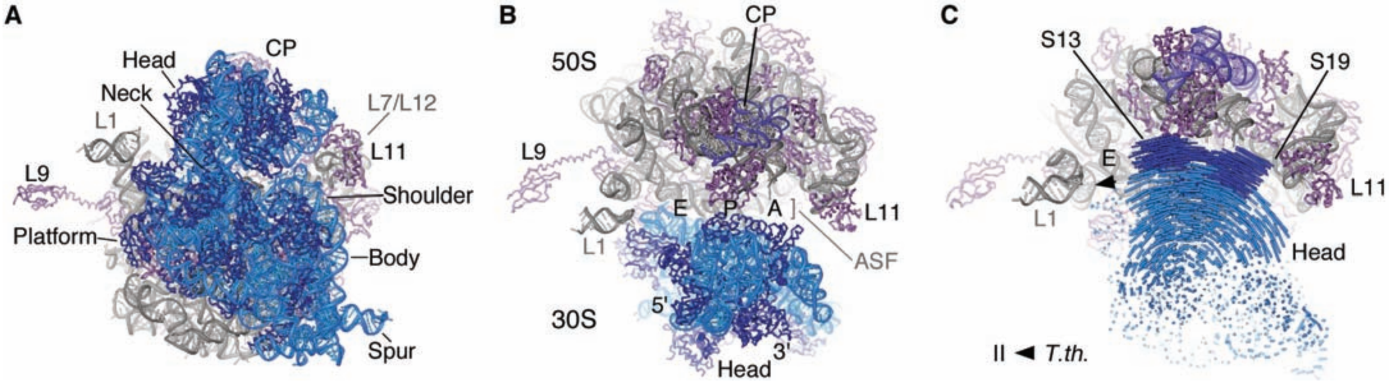

Fig. 1. Structure of intact *E. coli* 70*S* ribosome. (**A**) View from the solvent side of the 30*S* subunit. rRNA and proteins in the 30*S* subunit are colored light blue and dark blue, respectively. 23*S* rRNA and proteins in the 50*S* subunit are colored gray and magenta, respectively. 5*S* rRNA is colored purple. 30*S* features include head, neck, platform, body, shoulder, and spur. 50*S* features include L1 (protein L1/rRNA arm), CP (central protuberance), ASF (A-site finger), and L11 (protein L11/rRNA arm). The approximate location of proteins L7/L12 and the tip of the ASF, not observed in the structure, are in gray. (**B**) View rotated 90° about the horizontal axis in (A). Letters indicate the approximate alignments of the aminoacyl (A), peptidyl (P), and exit (E) tRNA binding sites at the subunit interface. The 5′ to 3′ direction of mRNA, which threads around the neck region of the 30*S* subunit, is also indicated. (**C**) Position of the head domain of the 30*S* subunit in ribosome II compared to the *T. thermophilus* 70*S* ribosome. Differences in the position of corresponding phosphorus atoms (light blue) and Cα positions for S13 and S19 (dark blue) in the two head domains are shown as vectors pointing in the direction of the arrows. The view is 60° about the horizontal axis in Fig. 1A.

(fig. S1) (*33*). In turn, the position of the head of the small subunit in ribosome I is rotated toward the E site by 6° when compared to the 5.5 Å structural models of the *Thermus thermophilus* 70*S* ribosome, which contain mRNA and tRNAs bound in the A and P sites (*15*) or in the P and E sites (*12*), respectively (fig. S1). Thus, the total rotation of the head that is observed in the three structures is about 12°, or 20 Å at the subunit interface (Fig. 1C).

The rotation of the head domain of the small subunit seen in the present structures parallels the trajectory of tRNAs through the ribosome and may provide a mechanism for controlling mRNA and tRNA movement during translocation. After peptide bond formation, the tRNAs move from the A and P sites in the pretranslocation state to the P and E sites in the posttranslocation state. The pretranslocation tRNAs occupy a hybrid state of binding (A/P and P/E sites) at least transiently before translocation is complete (Fig. 2A) (*37*). Recent biochemical evidence also suggests that mRNA and tRNA translocation requires an ''unlocking'' step on the small subunit (*30*, *31*, *38*). Peptide bond formation allows tRNA movement on the large subunit and permits a ratcheting motion of the subunits required for translocation (*16*, *21*, *27*, *38*, *39*) (Fig. 2B). Spahn *et al*. (*27*) proposed that subsequent rotation of the head of the small subunit (Fig. 2B) directs movement of the tRNAs to the P and E sites. However, the structural basis for the ''unlocking'' event remains unclear.

The present structures provide a detailed view of changes in the small subunit that allow swiveling of the head, and also suggest a mechanism for ''unlocking'' the small subunit to complete translocation. In comparisons between ribosomes I and II and the *T. thermophilus* 30*S* subunit, nearly all of the conformational changes responsible for the rigid-body rotation of the head are concentrated in four base pairs (nucleotides 929 to 932 paired with 1388 to 1385) in h28 of 16*S* rRNA (Fig. 2C) (*33*). It is noteworthy that six of the seven base pairs in helix h28 are G-C base pairs in most bacteria (fig. S2). This high G-C content is highly conserved across all kingdoms (*34*), which suggests that helix h28 may act as a stiff spring to absorb the strains induced by the rotation of the head domain (*40*).

When compared to previous results (*8*, *12*, *15*), the present structures reveal that the ''lock'' that must be opened during translocation is likely a steric block between the P and E sites on the small subunit. In all of the available structures, the path that A-site tRNA traverses to enter the P site is relatively unobstructed on the small subunit. In contrast, residues G1338 to U1341 in 16*S* rRNA form a stable ridge in the head of the small subunit (fig. S2) that sterically separates the anticodon stem-loop of P-site tRNA from the E site (*12*, *15*). In a 5.5 Å structure of the pretranslocation state (*15*) and in an 11 Å structure of a P/E hybrid state (*21*), the G1338-U1341 ridge in the head and A790 in the small-subunit platform leave a gap of only 12 to 13 Å (fig. S2); more than 20 Å would be needed for an A-form RNA helix to pass through. This ''lock'' in the small subunit seems to allow tRNA movement to the P/E hybrid state, but prevents complete translocation (*21*, *31*). The observed rotations of the head domain of the small subunit in ribosomes I and II do not increase the gap, and the head domain would retain tight packing with the P-site tRNA anticodon stem (Fig. 2D). Interestingly, the conformation of the 30*S* subunit in ribosome II resembles that of the 40*S* subunit in the yeast 80*S* ribosome bound to elongation factor eEF2 and sardorin, with respect to rotation of the head domain (*27*). However, the conformation of the 40*S* subunit in the yeast 80*S* ribosome–eEF2-sardorin complex opens the gap between the G1338-U1341 ridge and A790 to more than 20 Å, sufficient for P-site tRNA to move into the E site (Fig. 2E).

The mechanism for tRNA and mRNA translocation may therefore involve three types of movement within the small subunit: an overall ratcheting, swiveling of the head, and an opening of the tRNA binding groove to allow P-site tRNA to pass into the E site (Fig. 2B). Opening of the tRNA binding groove may represent unlocking of the small subunit, and this likely occurs physiologically only during or after guanosine triphosphate (GTP) hydrolysis by elongation factor EF-G (*21*, *30*, *31*). The precise ordering of these motions, however, will require new structural information about translocation intermediates.

Positions of the L1 and L11 arms in the 50*S* subunit. Two regions in the 50*S* subunit that change position as part of the translational elongation cycle are the L1 and L11 arms. The L11 arm contributes to the activity of initiation, elongation, and release factors (*18*, *19*, *21*–*23*, *25*, *41*–*43*), whereas the L1 arm is thought to influence movement of tRNA into and out of the E site (*12*, *21*). In the two *E. coli* ribosome structures, which lack bound tRNAs and translation factors, there are no contacts between these regions and the core of the ribosome that fix their respective positions. The different positions of the L1 and L11 arms in the two structures depend on conformational changes within RNA helices (fig. S3) (*33*). This means that three of the large-scale motions identified within the ribosome—movement of the L1 and L11 arms and swiveling of the head domain of the small subunit—depend on conformational changes

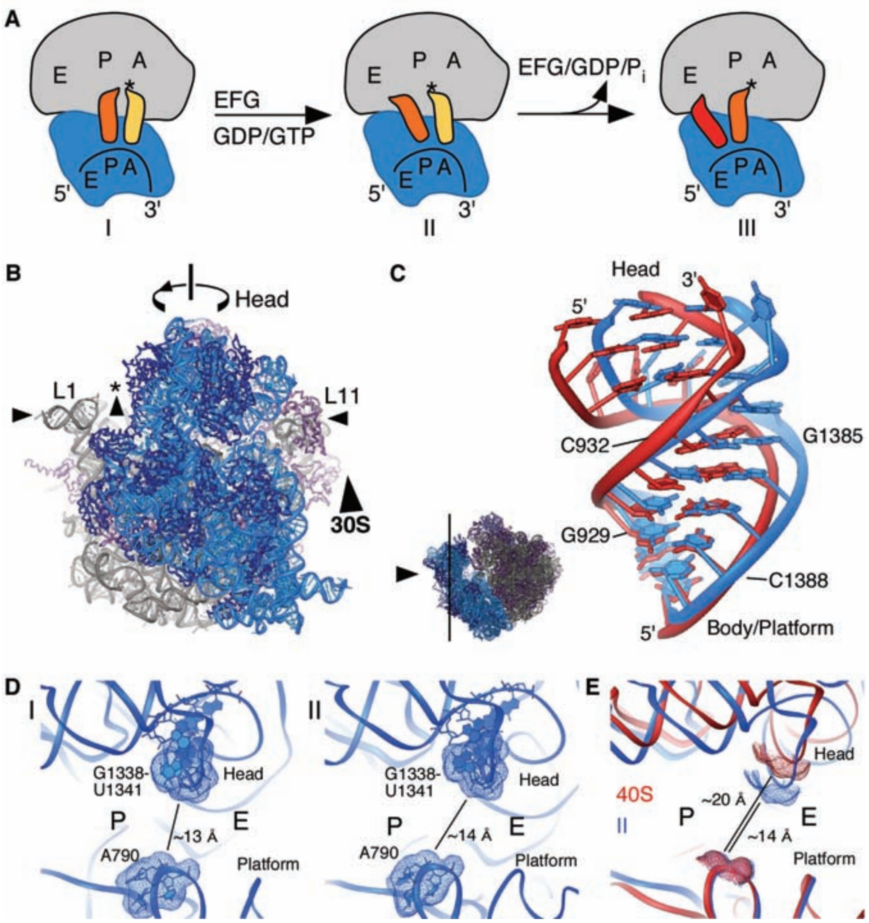

Fig. 2. Small-subunit tRNA binding sites and translocation intermediates. (**A**) Schematic steps in the mRNA and tRNA translocation reaction. After peptide bond formation, the pretranslocation complex (I) binds EF-G and shifts to the hybrid state of tRNA binding (complex II). Subsequent GTP hydrolysis by EF-G leads to the posttranslocation state (complex III). [Model abbreviated from (*31*)] (**B**) Model of structural changes in the ribosome that contribute to translocation, viewed as in Fig. 1A. Arrows indicate motions of the small and large subunit proposed to occur during the ratcheting mechanism: ratcheting of the small subunit, rotation of the small-subunit head domain, opening of the tRNA binding groove (asterisk), and lateral movements of the L1 and L11 arms (*16*, *21*, *27*). (**C**) View of the conformational differences in h28 of 16*S* rRNA in ribosomes I (blue) and II (red). The direction of view is indicated to the left. (**D**) View of the tRNA binding cleft in the 30*S* subunit, from the perspective of the large subunit. The G1338-U1341 ridge and A790, which separate the P and E sites, are marked. Molecular surfaces of the tRNA binding cleft in ribosome I (left) and ribosome II (right) are indicated. The shortest distance between the van der Waals surfaces is marked in each case. (**E**) Superposition of the 30*S* subunit in ribosome II (blue) with the yeast 40*S* subunit from the 80*S*-eEF2-sardorin complex (red) (*27*, *51*). Molecular surfaces and distances are shown as in Fig. 2D.

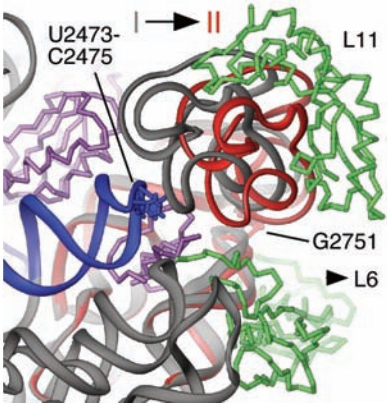

Fig. 3. Movement of the L11 arm in the two ribosomes. Nucleotides U2473 to C2475 in H89 and the tertiary contact with G2751 are marked. Proteins L6 and L11 from ribosome II are shown in green. Proteins L6 and L11 in ribosome I are not shown for clarity. The direction of movement of L6 is indicated by an arrowhead. The direction of view is that of Fig. 1A.

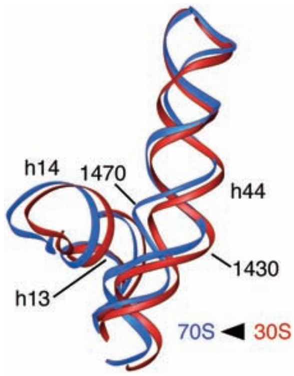

Fig. 4. Conformational changes in the 30*S* subunit when compared to the 70*S* ribosome. Helices h13, h14, and h44 in the 30*S* subunit (red) and 70*S* ribosome (blue) are shown from the interface side of the 30*S* subunit. Nucleotides and rRNA helices near the bend in h44 are marked.

within RNA helices, not on changes in tertiary structure.

When compared to ribosome II, the L11 arm in ribosome I has moved toward the tRNA binding sites at the subunit interface by about 15 Å (Fig. 3). This range of motion is the same as that observed in cryo-EM reconstructions of the yeast ribosome as part of the proposed mechanism of translocation (*27*). Similar but smaller conformational changes were observed in cryo-EM reconstructions of the *E. coli* ribosome in mRNA decoding intermediates (*18*, *22*). In the "closed" conformation observed in ribosome I, and also in the *T. thermophilus* 70*S* structures (*12*, *15*), loop nucleotides U2473 to C2475 at the end of H89 may act as a physical stop, preventing further movement inward toward the tRNA binding sites. On the other side, a tertiary interaction to G2751 in the loop of H97, also seen in the *Haloarcula marismortui* 50*S* structure (*10*), may limit outward movement of the L11 arm (Fig. 3) (fig. S3).

Comparisons to the 30*S* and 50*S* subunit structures. The overall conformations of the *H. marismortui*, *Deinococcus radiodurans*, and *E. coli* 50*S* subunits are remarkably similar (*33*). Apart from differences in the positions of the L1 and L11 arms, changes mainly reflect the mobility in 23*S* rRNA helices H69 and H34, and parts of proteins L2, L14, and L19 (*10*, *11*). These rRNA helices and proteins all reside in or near the subunit interface, as described below. By contrast, the 30*S* subunit (*8*) undergoes substantial rearrangement upon association with the 50*S* subunit (fig. S4). Conformational changes occur in the 30*S* subunit body and penultimate stem of 16*S* rRNA and in the relative position of the head and body domains with respect to the platform. The platform itself is nearly indistinguishable in the 30*S* and 70*S* structures (*33*). The head domain is also highly similar in the 30*S* and 70*S* structures (*33*), although, as noted previously, the head domain in each *E. coli* 70*S* ribosome is rotated toward the E site when compared to the 30*S* subunit.

Changes in the body of the small subunit when comparing 30*S* subunit structures to the 70*S* ribosome structures may be more relevant to the mechanism of translocation than to the mechanism of mRNA decoding. During mRNA decoding, the shoulder of the small subunit is thought to "close" around cognate, but not near-cognate or noncognate A-site tRNAs (*6*). The shoulder of the small subunit

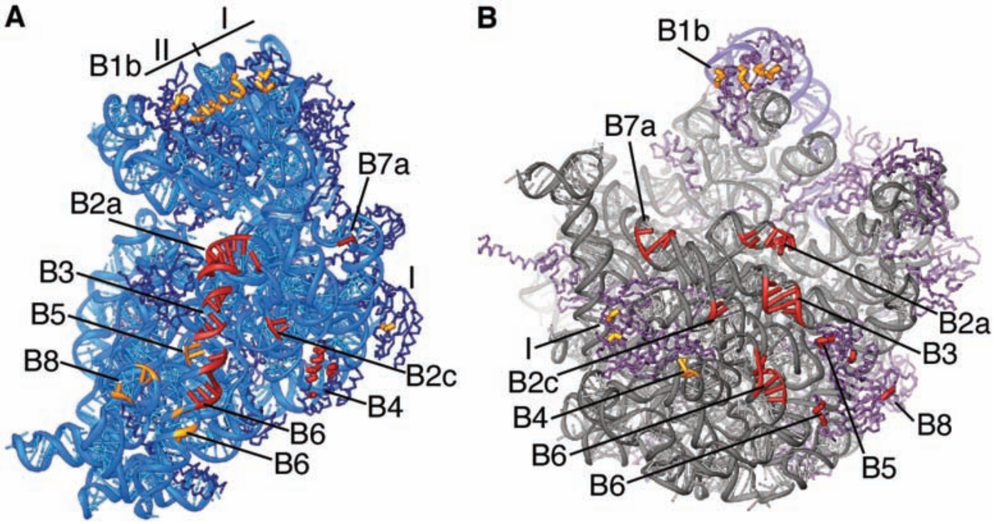

Fig. 5. Bridges between the 30*S* subunit and the 50*S* subunit. (**A**) Contacts at the interface of the 30*S* subunit, color-coded by type of interaction. Colors of rRNA and proteins are as described in Fig. 1A. Interactions that occur in only one of the two ribosomes are marked by ribosome (I or II). Interactions with protein in the opposite subunit, gold; interactions with RNA, red. (**B**) Contacts at the interface of the 50*S* subunit, color-coded by type of interaction as in (A).

in both 70*S* ribosomes adopts a conformation similar to that in the "open" 30*S* subunit structures (*6*), which suggests that subunit association has little effect on this structural rearrangement. By contrast, parts of helix h44 in 16*S* rRNA, the penultimate stem that runs along the body of the small subunit, and helices h8 and h14 are displaced laterally away from the platform side of the interface by 4 to 7 Å in the 70*S* ribosome structures when compared to the 30*S* subunit structure (fig. S4). The result is a penultimate stem that is less bowed in the 70*S* ribosome (Fig. 4). Helices h8, h14, and h44 are involved in a number of intersubunit contacts, as described below, which may explain the conformational differences. Consistent with this idea, the conformation of these helices in the *T. thermophilus* 70*S* ribosome structures seems to be the same as that seen here (*12*, *15*).

Interactions at the subunit interface. Previous structures of the ribosome have identified a number of intersubunit contacts, or bridges, that hold the ribosomal subunits together (*12*, *21*, *27*). In the present structures, the bridges at the subunit interface (Fig. 5) bury more than 6000 Å^2 of solvent-accessible surface area (*44*). However, a number of the intersubunit contacts have been proposed to rearrange, or even to break, as part of the elongation cycle (*12*, *21*, *27*). Apart from differences in the contacts to the head of the small subunit (described below), the bridges between the two ribosomal subunits at the interface are similar in the two structures of the *E. coli* ribosome. The RNA residues directly involved in subunit-subunit contacts superimpose with a root mean square deviation of less than 1 Å (*33*). When compared to the lower resolution ribosome structures, the interface between the body and platform of the 30*S* with the 50*S* subunit seen in the present structures adopts a conformation closest to that of the pretranslocation or posttranslocation state (complexes I or III in Fig. 2A) (*12*, *15*, *21*).

Two bridges between the head of the small subunit and the central protuberance of the large subunit in cryo-EM reconstructions are mirrored in the structures of the 70*S* ribosome presented here. In the first bridge [B1b/B1c in previous publications (*12*, *21*, *27*)], ribosomal proteins S13 and L5 contact each other. Protein S13 plays a key role in subunit association and in the fidelity of translocation because of its interactions with L5 in the central protuberance and with P-site tRNA (*8*, *21*, *45*–*47*). In both the pre- and posttranslocation states (*12*, *15*), L5 is directly across from the N-terminal globular domain of S13. In ribosome I, this contact is offset because S13 and the head of the small subunit are rotated toward the E site by several angstroms (Fig. 6A). The offset in ribosome I results in weak contact between S13, S19, and L5 (less than 400 Å^2 in buried surface area) (*33*), consistent with the dynamic nature of this interaction (*16*, *21*).

Strikingly, both the ratchet-like motion of the small subunit in the 70*S*/EF-G/GMPPNP [guanosine 5′-(β,γ-imido)triphosphate] complex (*21*) and the swivel motion of the head domain in ribosome II, although mechanically different, result in similar contacts between S13, S19, and L5. In ribosome II, the long α helix extending from the globular domain of S13 and running along the head of the small subunit forms a "rail" that lies in a shallow groove in protein L5 (Fig. 6B). Interactions between the three proteins are not extensive (<800 Å^2 buried surface area) (*33*), consistent with the observation that the contact rearranges during translocation (*16*, *21*).

The other bridge between the head of the small subunit and the large subunit, bridge B1a, includes the ASF (or H38 in 23*S* rRNA), which spans the subunit interface parallel to the A and P sites (Fig. 1B). This contact is not visible in the present structures because of disorder at the end of the ASF in both ribosomes I and II. Bridge B1a is clearly visible in the *T. thermophilus* ribosome structures and in posttranslocation complexes imaged by cryo-EM (*12*, *15*, *21*). However, in an interesting parallel to the structures of ribosomes I and II, this contact is visibly weakened in the cryo-EM reconstruction of the EF-G/GMPPNP posttermination complex (*21*). The dynamics of the ASF contact due to rotation of the head of the small subunit and the ratchet motion may aid movement of A-site tRNA into the P site. The antibiotic viomycin, which inhibits translocation, protects nucleotides near the base of the ASF from chemical modification (*48*); this finding supports a role for the ASF in translocation.

Interpretations of cryo-EM reconstructions identify two possible pivot points on either side of intersubunit bridge B3 for the ratcheting of the small subunit relative to the large subunit (*21*, *27*) (Fig. 5). Bridge B3 contains the largest RNA-RNA minor-groove surface complementarity among the interface contacts, which may preclude large rearrangements in this bridge during translocation. Bridge B3 may therefore serve as the pivot point of the ratcheting motion. In bridge B3, two sheared G-A base pairs in h44 of 16*S* rRNA form a type I A-minor interaction (*49*) with two G-C base pairs in H71 of 23*S* rRNA in the large subunit (Fig. 6C) (fig. S5). As observed in other type I A-minor interactions, nearly all hydrogen bonds are satisfied by the close packing interaction. Energetic contributions to similar contacts within a group I self-splicing intron and during mRNA decoding suggest that surface complementarity helps to stabilize association, whereas hydrogen bonding compensates for desolvation (*50*, *51*).

At the apex of the small-subunit platform, bridge B7a (Fig. 5) involves the only cross-subunit base stacking interaction, between A702 in h23 of 16*S* rRNA and A1848 in H68 of 23*S* rRNA. In combination with A1848, A702 forms a variant of the A-minor motif (*49*) in which the adenosines pack against adjacent C-G base pairs in H68 of 23*S* rRNA (Fig. 6D) (fig. S5). Interestingly,

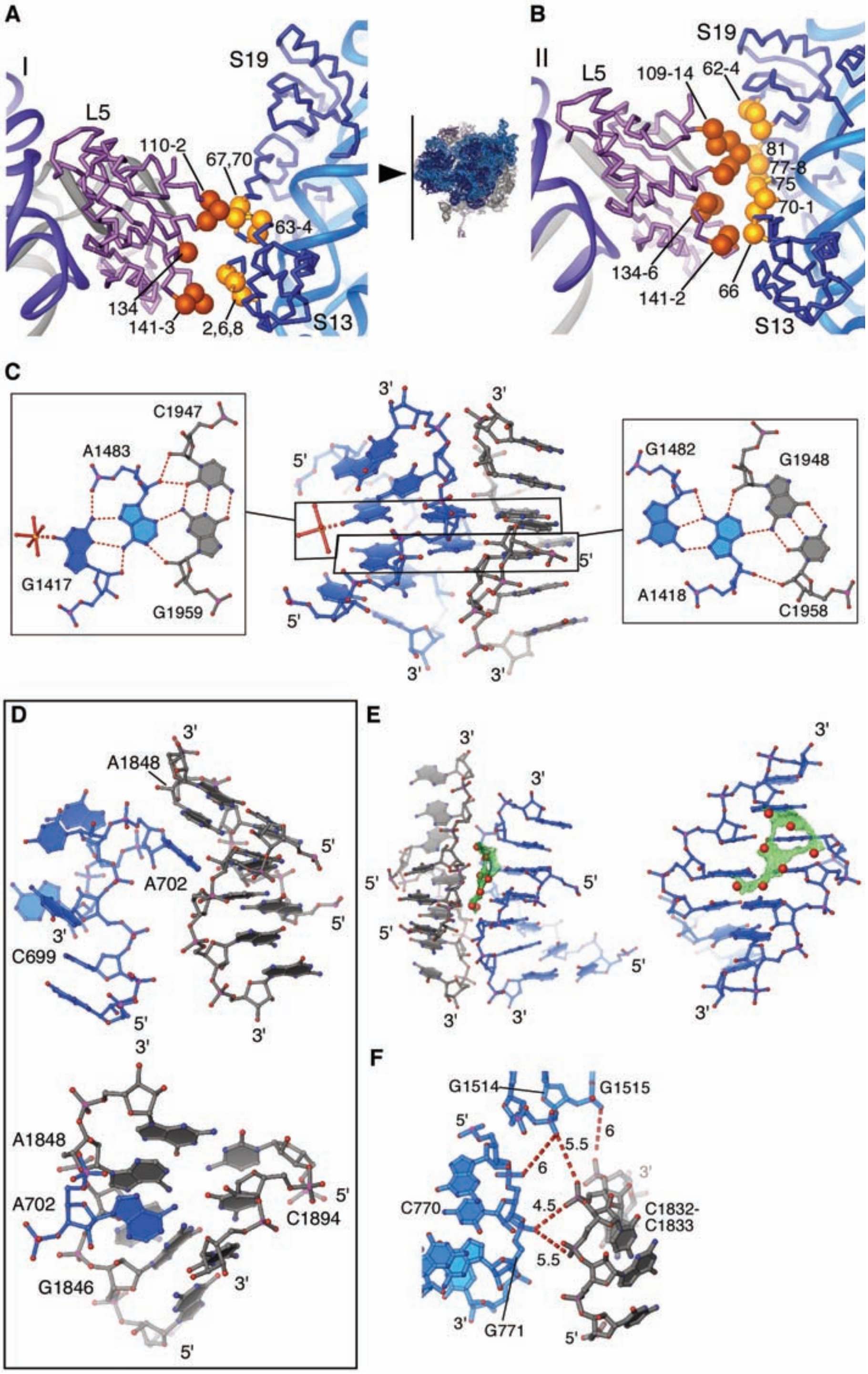

Fig. 6. Molecular interactions in the intersubunit bridges. (**A**) Contact between S13 and L5 in ribosome I. (**B**) Contact between S13 and L5 in ribosome II. Only the Cα traces for the proteins are shown, because protein side chains are not clear in the electron density of either ribosome. Residues that become inaccessible to solvent (*44*) are indicated in orange for L5 and in yellow for S13 and S19. The direction of view is indicated in the center. (**C**) Molecular interactions in bridge B3. (**D**) Molecular interactions in bridge B7a. (**E**) Molecular interactions in bridge B6. Waters modeled at the interface are shown as red spheres inside the water-accessible volume, green mesh. (**F**) Close approach of phosphates at the subunit interface near bridge B2c. Distances (in angstroms) between phosphate oxygens are marked.

the helical geometry in this region of 23*S* rRNA is conserved between archaea (*10*) and bacteria, whereas the residue at position 702 in 16*S* rRNA is kingdom-specific (*34*). In the ratchet-like motion (Fig. 2B), the interface in this region shifts by at least 6 Å laterally with respect to H68 (*21*, *27*), indicating that this contact must break during translocation.

In striking contrast to the desolvated nature of bridge B3, the neighboring bridge B6, between h44 in 16*S* rRNA and H62 in 23*S* rRNA, buries a large surface area that is almost entirely solvated. The minor grooves of h44 and H62 contact each other sparingly and leave a 6 Å gap that can accommodate a monolayer of water molecules (Fig. 6E) (fig. S5) (*33*). These water molecules can all be positioned within 3 Å of minor-groove hydrogen bond donors and acceptors in both subunits. Interestingly, many previously identified bridges between the center of the small-subunit platform and the large subunit are also highly solvated (*12*) (Fig. 5). There are many instances where phosphate groups from both subunits lie within 4 to 6 Å of each other (Fig. 6F), suggesting that nonspecific ions form part of the interface solvation network (*52*). Other bridges that contribute only small regions of direct contact in the present structures are described in (*33*). The high level of solvation at the subunit interface may be necessary to allow ratcheting during translocation, where the relative orientation of the two subunits may change by 7° to 10° (*21*, *27*).

Bridges B2a and B4 occur between the 30*S* platform and the 50*S* subunit (Fig. 5) and are essential for subunit association (*53*). Bridge B2a occurs at the functional center of the ribosomal interface and is immediately adjacent to the mRNA decoding site, between the top of h44 in 16*S* rRNA and H69 in 23*S* rRNA, and extends under the P site toward h45 and h24 (*12*, *18*, *22*). During mRNA decoding, the closing loop of H69 resides immediately below the D stem of A-site tRNA, whereas the adjacent stem of H69 is located below the D stem of P-site tRNA (*12*, *18*, *22*). H69 moves laterally with respect to the small subunit by 6 to 8 Å during the ratchet-like motion of the small subunit during translocation (*21*). Furthermore, ribosome recycling factor (RRF) causes the tip of H69 to peel away from the 30*S* subunit as part of the subunit dissociation process (*24*, *54*, *55*). The present structures provide a detailed view of H69 in the context of the 70*S* ribosome.

In the two *E. coli* ribosome structures, the base of H69 is identical in conformation through base pair Ψ1911/A1919. The loop at the end of H69 has slightly different conformations in the two ribosomes, possibly because of tighter packing at the interface between h44 and H69 in ribosome II when compared to ribosome I (fig. S5). However, a number of noncanonical base pairs in the loop that likely contribute to subunit association is conserved in the two structures. A widened reversed-Hoogsteen base pair between Ψ1911 and A1919, bridged by the 2′-OH of A1918, allows A1918 and A1919 to form an A-A dinucleotide platform (*56*) (Fig. 7A). This projects A1919 into the minor groove of h44 near bases U1406/U1495, where it also interacts with the base of

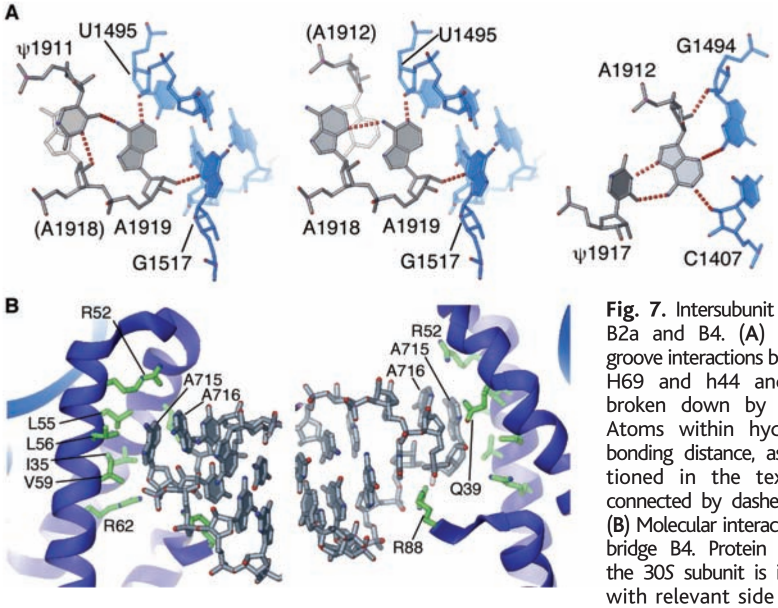

Fig. 7. Intersubunit bridges B2a and B4. (**A**) Minor-groove interactions between H69 and h44 and h45, broken down by region. Atoms within hydrogen-bonding distance, as mentioned in the text, are connected by dashed lines. (**B**) Molecular interactions in bridge B4. Protein S15 in the 30*S* subunit is in blue, with relevant side chains in green. The interaction is viewed from the left side of Fig. 5A (left) and from the right side of Fig. 5A (right). Electron density is visible for the side chain of Arg^{88} (R88) in ribosome II, but not in ribosome I. Other amino acid abbreviations: I, Ile; L, Leu; V, Val; A, Ala; Q, Gln.

G1517 (Fig. 7A). Nucleotide A1912, which stacks on A1918 and forms a distorted reversed-Hoogsteen base pair with Ψ1917, projects into the minor groove of base pair C1407/G1494 in h44 of 16*S* rRNA (Fig. 7A). The involvement of all three N1 positions of A1912, A1918, and A1919 in packing interactions is consistent with interference of subunit association when these residues are N1-methylated by dimethyl sulfate (*53*). Other details of the bridge B2a interactions are given in (*33*).

Bridge B4 near the base of the platform likely remains intact even during the ratchet-like motion of translocation (*27*). Bridge B4 involves stem-loop H34 in 23*S* rRNA and protein S15 in the small subunit (*57*) (Fig. 5). H34 extends from the surface of the 50*S* subunit by about 30 Å and has been observed in different orientations in the isolated 50*S* subunit structures (*10*, *11*). This helix is nearly 60 Å from the putative pivot point of the ratchet-like motion between subunits (bridge B3, Fig. 5), which may explain the need for its flexibility in order to maintain intersubunit interactions. In the contact, the closing loop of H34 forms a U-turn in which A715 packs against a hydrophobic surface on S15 (Fig. 7B) (fig. S5). In addition, Gln^{39} and Arg^{88} of S15 interact with the minor and major grooves of the loop nucleotides, respectively. Methylation of the N1 position of A715 has been shown to interfere with subunit association (*53*). Interestingly, the N1 position of A715 is not in direct contact with any residue of either subunit, but is 4 to 5 Å from the guanidinium group of Arg^{52} in S15. The interference may therefore be due to a positive charge on 1-methyladenosine (*58*), which would lead to charge-charge repulsion with Arg^{52}.

Magnesium ion binding sites in the 70*S* ribosome. Formation of the 70*S* ribosome and the process of protein synthesis are highly dependent on the concentration of divalent metal ions in vitro (*59*–*61*). Some of the magnesium dependence is likely due to the close approach of phosphates at the interface, as described above (Fig. 6F) (*52*). Interestingly, most of the specific magnesium ion binding sites identified in the 30*S* subunit within the 70*S* ribosome are identical to those in the isolated 30*S* subunit (*62*) (fig. S7), despite sequence differences between the *T. thermophilus* and *E. coli* ribosomes and the conformational changes that occur upon subunit association (Fig. 4) (fig. S4). Comparisons to the *H. marismortui* 50*S* subunit reveal that about 40% of the Mg^{2+} binding sites are conserved across kingdoms and upon subunit association (*63*) (fig. S7). Most of the Mg^{2+} ions that are conserved involve one to four inner-sphere coordination sites to rRNA phosphate oxygens and electronegative groups on the bases (N7 of purines, O6 of guanosines, O4 and O2 of uridine, and O2 of cytidine). The networks of conserved Mg^{2+} binding sites indicate that magnesium ion cores are a conserved part of RNA tertiary structure within the ribosome (*63*, *64*).

Comparison with the 30*S* and 50*S* subunit structures reveals only one clear example of a specific magnesium ion binding site that becomes occupied when the subunits associate to form the 70*S* ribosome. This site occurs in the major groove of contact B3 (Fig. 6C). In the structure of the *T. thermophilus* 30*S* subunit, a fully hydrated Mg^{2+} site occurs adjacent to the tandem sheared G-A base pairs (*8*). Upon subunit association, this Mg^{2+} moves to adopt inner-sphere coordination with G1417 (Fig. 6C). The sequence of 16*S* rRNA near the ion is identical in *T. thermophilus* and in *E. coli* (*34*), ruling out sequence-dependent effects.

Conformation of the peptidyl transferase center. The peptidyl transferase center (PTC) of the ribosome is located in the large ribosomal subunit at the base of a cleft that binds the acceptor ends of tRNAs (*3*, *10*). Although isolated 50*S* subunits are active in peptide bond formation, the rate of catalysis on 50*S* subunits is lower than that of intact 70*S* ribosomes by a factor of about 1000 (*65*, *66*). The mechanism used by the ribosome to accelerate peptide bond formation is thought to be due almost entirely to substrate positioning within the active site (*67*, *68*), coupled to substrate-assisted catalysis (*69*). This suggests that conformational differences in the intact ribosome, when compared to isolated 50*S* subunits, may be responsible in large part for the differences in the observed rates of peptidyl transfer.

In the two 70*S* ribosomes, the PTCs are nearly identical in conformation (*33*). Comparison of the *E. coli* and *D. radiodurans* structures indicates that the overall conformation of the PTC is more closed in the 50*S* subunit than in the 70*S* ribosome, because of movement of both P-site and A-site residues toward the geometric center of the PTC (*11*) (Fig. 8A). In the *D. radiodurans* 50*S* subunit structure, the P-loop bases responsible for base pairing to the CCA end of P-site tRNA (G2251 and G2252), as well as nucleotides 2062 and 2063, are shifted laterally toward the A site, whereas nucleotides U2584 and U2506 on the A-site side are shifted toward the P-site side of the PTC.

The PTC of the *H. marismortui* 50*S* subunit is also more closed relative to that in the 70*S* ribosome (*3*, *5*, *33*, *70*). However, in this case the P-site side of the PTC is essentially identical, whereas in the *E. coli* 70*S* ribosome structures, nucleotide U2506 on the A-site side has shifted toward base A2451 at the side of the PTC, and U2584 is rotated away from A2451 (Fig. 8, B and C). A shift of U2506 toward A2451 would have a substantial impact on the positioning of A76 in the A-site tRNA, because of its interactions with the base pair between U2506 and G2583 in 23*S* rRNA. A76 would have to move toward the A2451 strand by 1.5 to 2 Å to avoid steric clashes and to form hydrogen bonds with the minor-groove face of the nucleotide (Fig. 8C). Note that the difference in conformation between the PTC in the *H. marismortui* 50*S* subunit and in the *E. coli* 70*S* ribosome does not seem to be driven by changes at the subunit interface. Instead, the position of the factor binding site region (H91 and H95 in 23*S* RNA) of the *H. marismortui* 50*S* subunit is moved toward the subunit interface, which in turn affects the position of the U2506 rRNA strand and the A-loop that forms a base pair with C75 of A-site tRNA (*3*, *5*, *70*–*72*).

In the 70*S* ribosome, some degree of flexibility in U2506 can be detected in one of

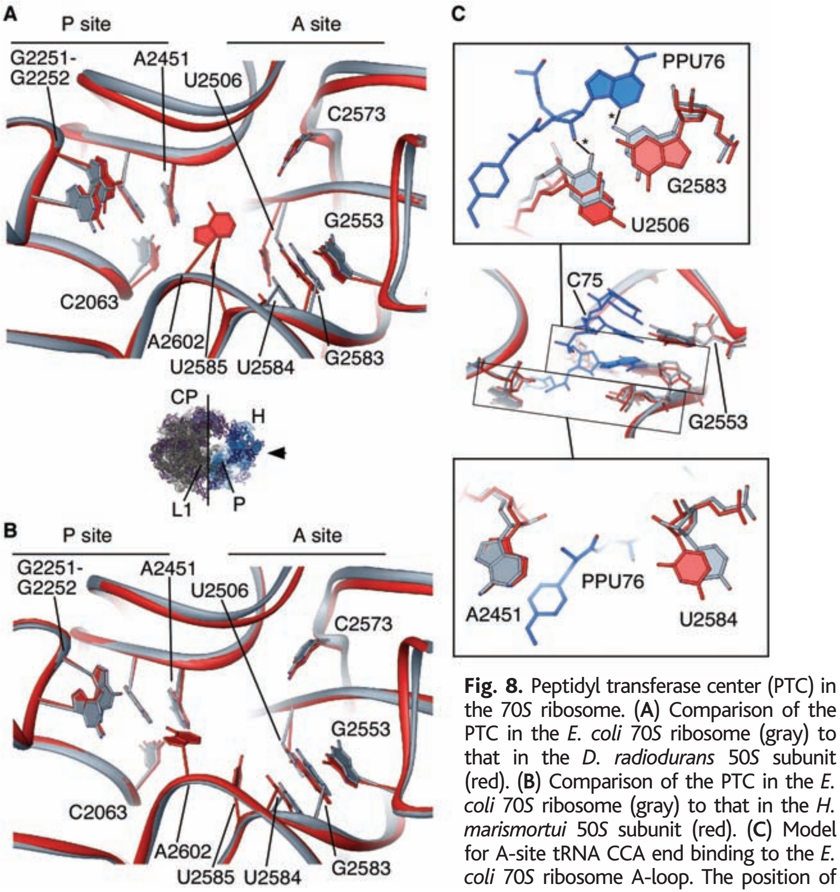

Fig. 8. Peptidyl transferase center (PTC) in the 70*S* ribosome. (**A**) Comparison of the PTC in the *E. coli* 70*S* ribosome (gray) to that in the *D. radiodurans* 50*S* subunit (red). (**B**) Comparison of the PTC in the *E. coli* 70*S* ribosome (gray) to that in the *H. marismortui* 50*S* subunit (red). (**C**) Model for A-site tRNA CCA end binding to the *E. coli* 70*S* ribosome A-loop. The position of CCA bound to the *H. marismortui* 50*S* subunit was docked on the basis of superposition of the entire PTC (*33*). Asterisks indicate minor-groove interactions of ~2 Å, if A76 is not shifted to account for the shifts in the *E. coli* rRNA.

the two ribosome structures, where electron density for the base is missing in simulated annealing omit electron density maps for ribosome I (fig. S8). This base is flipped out of the base pair, with G2583 toward U2585 in one *H. marismortui* 50*S* subunit structure with bound CCA trinucleotide substrate analogs (*5*), and is not paired in the *D. radiodurans* structure (*11*). Furthermore, two critical PTC nucleotides in the innermost layer surrounding the CCA ends of the tRNA substrates (*3*, *69*) are disordered in the 70*S* ribosome (bases of U2585 and A2602; fig. S8). These nucleotides adopt different conformations depending on the nature of the substrates bound in the 50*S* subunit structures (*3*, *5*, *70*, *73*). The degree of flexibility seen in the 70*S* ribosome PTC, along with a more "open" conformation, may contribute to more rapid peptide bond formation in the 70*S* ribosome relative to the 50*S* subunit.

Conclusion. Comparisons of the two structures of the *E. coli* ribosome to previously determined x-ray crystal structures and cryo-EM reconstructions indicate that the EF-G–catalyzed unlocking event during translocation (*30*, *31*) involves opening of the G1338-U1341 ridge between the P and E sites on the small subunit. This model can now be tested. The degree to which large-scale motions in the ribosome are concentrated in RNA helices is surprising, given the universal conservation of nearby residues (*34*). High-resolution structures of the ribosome in the different functional states that drive these large-scale movements will be needed to determine how they are controlled. Also noteworthy is the high level of solvation at the subunit interface, especially in the center of the small-subunit platform and in bridge B6 (*12*). The functional roles of such an interface and how the interface rearranges during translocation remain to be determined.

References and Notes

1. V. Ramakrishnan, *Cell* **108**, 557 (2002).
2. P. Khaitovich, A. S. Mankin, R. Green, L. Lancaster, H. F. Noller, *Proc. Natl. Acad. Sci. U.S.A.* **96**, 85 (1999).
3. P. Nissen, J. Hansen, N. Ban, P. B. Moore, T. A. Steitz, *Science* **289**, 920 (2000).
4. R. Green, H. F. Noller, *Annu. Rev. Biochem.* **66**, 679 (1997).
5. T. M. Schmeing, P. B. Moore, T. A. Steitz, *RNA* **9**, 1345 (2003).
6. J. M. Ogle, V. Ramakrishnan, *Annu. Rev. Biochem.* **74**, 129 (2005).
7. P. B. Moore, T. A. Steitz, *Annu. Rev. Biochem.* **72**, 813 (2003).
8. B. T. Wimberly *et al.*, *Nature* **407**, 327 (2000).
9. F. Schluenzen *et al.*, *Cell* **102**, 615 (2000).
10. N. Ban, P. Nissen, J. Hansen, P. B. Moore, T. A. Steitz, *Science* **289**, 905 (2000).
11. J. Harms *et al.*, *Cell* **107**, 679 (2001).
12. M. M. Yusupov *et al.*, *Science* **292**, 883 (2001); published online 29 March 2001 (10.1126/science.1060089).
13. G. Z. Yusupova, M. M. Yusupov, J. H. Cate, H. F. Noller, *Cell* **106**, 233 (2001).
14. A. Vila-Sanjurjo *et al.*, *Proc. Natl. Acad. Sci. U.S.A.* **100**, 8682 (2003).
15. L. Jenner *et al.*, *Science* **308**, 120 (2005).
16. J. Frank, R. K. Agrawal, *Nature* **406**, 318 (2000).
17. H. Stark, M. V. Rodnina, H. J. Wieden, M. van Heel, W. Wintermeyer, *Cell* **100**, 301 (2000).
18. H. Stark *et al.*, *Nat. Struct. Biol.* **9**, 849 (2002).
19. B. P. Klaholz *et al.*, *Nature* **421**, 90 (2003).
20. U. B. Rawat *et al.*, *Nature* **421**, 87 (2003).
21. M. Valle *et al.*, *Cell* **114**, 123 (2003).
22. M. Valle *et al.*, *Nat. Struct. Biol.* **10**, 899 (2003).
23. B. P. Klaholz, A. G. Myasnikov, M. Van Heel, *Nature* **427**, 862 (2004).
24. N. Gao *et al.*, *Mol. Cell* **18**, 663 (2005).
25. G. S. Allen, A. Zavialov, R. Gursky, M. Ehrenberg, J. Frank, *Cell* **121**, 703 (2005).
26. R. Beckmann *et al.*, *Cell* **107**, 361 (2001).
27. C. M. Spahn *et al.*, *EMBO J.* **23**, 1008 (2004).
28. M. Halic *et al.*, *Nature* **427**, 808 (2004).
29. J. F. Menetret *et al.*, *J. Mol. Biol.* **348**, 445 (2005).
30. A. Savelsbergh *et al.*, *Mol. Cell* **11**, 1517 (2003).
31. A. V. Zavialov, V. V. Hauryliuk, M. Ehrenberg, *J. Biol.* **4**, 9 (2005).
32. G. Blaha *et al.*, *Methods Enzymol.* **317**, 292 (2000).
33. See supporting data on *Science* Online.
34. J. J. Cannone *et al.*, *BMC Bioinformatics* **3**, 2 (2002).
35. B. Boeckmann *et al.*, *Nucleic Acids Res.* **31**, 365 (2003).
36. J. Frank, *Biopolymers* **68**, 223 (2003).
37. D. Sharma, D. R. Southworth, R. Green, *RNA* **10**, 102 (2004).
38. A. Spirin, *Biochimie* **69**, 949 (1987).
39. A. V. Zavialov, M. Ehrenberg, *Cell* **114**, 113 (2003).
40. P. J. Hagerman, *Annu. Rev. Biophys. Biomol. Struct.* **26**, 139 (1997).
41. W. P. Tate, H. Schulze, K. H. Nierhaus, *J. Biol. Chem.* **258**, 12816 (1983).
42. D. Mohr, W. Wintermeyer, M. V. Rodnina, *Biochemistry* **41**, 12520 (2002).
43. L. Brandi *et al.*, *J. Mol. Biol.* **335**, 881 (2004).
44. A. T. Brünger *et al.*, *Acta Crystallogr. D* **54**, 905 (1998).
45. A. R. Cukras, D. R. Southworth, J. L. Brunelle, G. M. Culver, R. Green, *Mol. Cell* **12**, 321 (2003).
46. A. R. Cukras, R. Green, *J. Mol. Biol.* **349**, 47 (2005).
47. L. Hoang, K. Fredrick, H. F. Noller, *Proc. Natl. Acad. Sci. U.S.A.* **101**, 12439 (2004).
48. D. Moazed, H. F. Noller, *Biochimie* **69**, 879 (1987).
49. P. Nissen, J. A. Ippolito, N. Ban, P. B. Moore, T. A. Steitz, *Proc. Natl. Acad. Sci. U.S.A.* **98**, 4899 (2001).
50. D. J. Battle, J. A. Doudna, *Proc. Natl. Acad. Sci. U.S.A.* **99**, 11676 (2002).
51. J. M. Ogle, F. V. Murphy, M. J. Tarry, V. Ramakrishnan, *Cell* **111**, 721 (2002).
52. D. E. Draper, *RNA* **10**, 335 (2004).
53. U. Maivali, J. Remme, *RNA* **10**, 600 (2004).
54. R. K. Agrawal *et al.*, *Proc. Natl. Acad. Sci. U.S.A.* **101**, 8900 (2004).
55. D. N. Wilson *et al.*, *EMBO J.* **24**, 251 (2005).
56. J. H. Cate *et al.*, *Science* **273**, 1696 (1996).
57. G. M. Culver, J. H. Cate, G. Z. Yusupova, M. M. Yusupov, H. F. Noller, *Science* **285**, 2133 (1999).
58. J. B. Macon, R. Wolfenden, *Biochemistry* **7**, 3453 (1968).
59. G. H. Hoa *et al.*, *Biochemistry* **19**, 3080 (1980).
60. P. C. Jelenc, C. G. Kurland, *Proc. Natl. Acad. Sci. U.S.A.* **76**, 3174 (1979).
61. K. B. Gromadski, M. V. Rodnina, *Mol. Cell* **13**, 191 (2004).
62. F. V. Murphy, V. Ramakrishnan, A. Malkiewicz, P. F. Agris, *Nat. Struct. Mol. Biol.* **11**, 1186 (2004).
63. D. J. Klein, P. B. Moore, T. A. Steitz, *RNA* **10**, 1366 (2004).
64. J. H. Cate, R. L. Hanna, J. A. Doudna, *Nat. Struct. Biol.* **4**, 553 (1997).
65. R. E. Monro, *J. Mol. Biol.* **26**, 147 (1967).
66. V. I. Katunin, G. W. Muth, S. A. Strobel, W. Wintermeyer, M. V. Rodnina, *Mol. Cell* **10**, 339 (2002).
67. A. Sievers, M. Beringer, M. V. Rodnina, R. Wolfenden, *Proc. Natl. Acad. Sci. U.S.A.* **101**, 7897 (2004).
68. E. M. Youngman, J. L. Brunelle, A. B. Kochaniak, R. Green, *Cell* **117**, 589 (2004).
69. J. S. Weinger, K. M. Parnell, S. Dorner, R. Green, S. A. Strobel, *Nat. Struct. Mol. Biol.* **11**, 1101 (2004).
70. J. L. Hansen, T. M. Schmeing, P. B. Moore, T. A. Steitz, *Proc. Natl. Acad. Sci. U.S.A.* **99**, 11670 (2002).
71. R. R. Samaha, R. Green, H. F. Noller, *Nature* **377**, 309 (1995).

72. D. F. Kim, R. Green, *Mol. Cell* **4**, 859 (1999).
73. A. Bashan *et al.*, *Mol. Cell* **11**, 91 (2003).
74. We thank J. Plecs, K. Frankel, G. Hura, and G. Meigs for help with data measurement at the SIBYLS and 8.3.1 beamlines at the Advanced Light Source; J. Frank for providing the cryo-EM reconstructions of the *E. coli* 70*S* ribosome; W. Ridgeway for rapid crystallization screen designs; A. Borovinskiy for help with protein modeling; and J. Doudna, P. Adams, V. Ramakrishnan, H. Noller, and R. Green for helpful discussions and comments on the manuscript. A.V.-S. acknowledges F. Vila for balance and coherence. Atomic coordinates and structure factors are deposited in the Protein Data Bank (accession codes 2AVY, 2AW4, 2AW7, and 2AWB). Supported by NIH grant GM65050 (J.H.D.C.), National Cancer Institute grant CA92584 (for the SIBYLS and 8.3.1 beamlines), and U.S. Department of Energy grants DE-AC03-76SF00098, KP110201, and LBNL LDRD 366851 (J.H.D.C.) and DE-AC03 76SF00098 (for the SIBYLS and 8.3.1 beamlines).

Supporting Online Material
www.sciencemag.org/cgi/content/full/310/5749/827/DC1
Materials and Methods
Figs. S1 to S8
Tables S1 to S3
References

11 July 2005; accepted 10 September 2005
10.1126/science.1117230

REPORTS

The Onset of Planet Formation in Brown Dwarf Disks

Dániel Apai,[1,2]*† Ilaria Pascucci,[1]* Jeroen Bouwman,[3]
Antonella Natta,[4] Thomas Henning,[3] Cornelis P. Dullemond[3]

The onset of planet formation in protoplanetary disks is marked by the growth and crystallization of sub–micrometer-sized dust grains accompanied by dust settling toward the disk mid-plane. Here, we present infrared spectra of disks around brown dwarfs and brown dwarf candidates. We show that all three processes occur in such cool disks in a way similar or identical to that in disks around low- and intermediate-mass stars. These results indicate that the onset of planet formation extends to disks around brown dwarfs, suggesting that planet formation is a robust process occurring in most young circumstellar disks.

Planet formation starts with the growth of sub-micrometer-sized amorphous grains in the protoplanetary disks [e.g., (*1*, *2*)]. Theory predicts that larger grains settle faster to the disk mid-plane, resulting in flattened disk geometries [e.g., (*2*, *3*)]. Observational evidence for dust settling has been found for disks around young, low-mass (T Tauri) and intermediate-mass (Herbig Ae/Be) stars [e.g., (*4*)]. Substantial dust processing in the early solar system is demonstrated by the high crystallinity of some comets containing dust from the epoch of their formation (*5*). Recently, intermediate-mass stars were shown to have high crystallinity only when larger grains are present (*6*), suggesting a possible link between grain growth and crystallization. Up to now, detailed dust composition studies were limited to bright disks of intermediate-mass stars, which suggested very low or no crystallinity for disks around low-mass stars [e.g., (*6*)]. If true, dust processing would strongly depend on the stellar properties, and planet formation processes would differ or not occur at all in disks of very-low-mass stars. Recently, accumulating evidence indicates that crystalline silicates are present in disks of low-mass stars [e.g., (*7*, *8*)]. Even more surprisingly, ground-based photometry of a brown dwarf disk showed hints for grain growth and dust settling (*9*), and crystalline silicate features were identified in the disk of a brown dwarf candidate (*10*). These findings set the question of whether such few Jupiter-mass disks (*11*, *12*) can form planets. In this report, we present mid-infrared spectra of disks around very-low-mass young stellar and substellar objects. We show that five out of six disks have highly processed dust: Large grains and very high crystalline mass fractions ($\sim$40%) are found. The correlation between the shape and strength of the silicate emission feature observed for Herbig Ae/Be disks extends to brown dwarf disks, demonstrating that dust processing is independent of the stellar properties. All the disks with highly processed dust have strongly flattened disk structure, as expected from dust settling. We conclude that the first steps of planet formation occurred in these brown dwarf disks, suggesting that even substellar disks can form planets.

We used the Spitzer Space Telescope and its sensitive Infrared Spectrograph to survey the complete population of substellar-mass objects with previously identified mid-infrared excess emission (*13*, *14*) in the Chamaeleon I star-forming region. We obtained low-resolution ($\lambda/\Delta\lambda \sim 60$ to 120) infrared spectra between 7.7 and 14.4 μm, covering the 10-μm silicate emission feature, whose shape and strength is determined by dust grain size and composition. Our targets have been spectroscopically classified as brown dwarf candidates or objects on the stellar-substellar boundary (*13*–*16*). The observations provide a yet-unique coeval sample (1 to 3 My) of cool objects with temperatures between 2500 and 3100 K, expanding the range in stellar mass over which dust composition has been studied to two orders of magnitude, a factor of two in temperature, and four orders of magnitude in luminosity. The spectra were taken by using multiple ramp cycles and reduced with the Spectroscopic Modeling, Analysis, and Reduction Tool (SMART) reduction package and routines we developed (*16*, *17*). We confirm mid-infrared excess emission, indicative of disks, for six of our targets; the fluxes of the two other objects (Cha 449 and Cha 425) are consistent with pure photospheric emission and are excluded from further analysis.

The spectra allow morphological comparison with the infrared spectrum of the interstellar medium and that of comet Hale-Bopp, as shown in Fig. 1. All six brown dwarf disks have emission features substantially broader than that of the interstellar medium, indicative of larger grains [e.g., (*18*)]. Whereas the spectrum of Cha Hα1 peaks at 9.8 μm, similarly to the dominantly amorphous interstellar grains, the other five targets show prominent crystalline silicate emission features with characteristic peaks at 9.3 μm and 11.3 μm. In particular, the spectrum of Cha 410 resembles that of comet Hale-Bopp. The faintest of our targets, Cha Hα9, shows a strong crystalline contribution, but because of its low signal-to-noise ratio we excluded it from the further quantitative analysis. To link grain growth and crystallization (*7*, *19*), we studied the relationship between the strength and the shape of the silicate feature by plotting the flux ratio at 11.3 μm and 9.8 μm against the peak over continuum flux ratio (Fig. 2). To ensure homogeneity, we used a single procedure to derive these values for young intermediate-mass stars (*6*), low-mass stars (*7*), and our brown dwarf sample. For intermediate-mass stars, a linear correlation has been proposed by (*6*): Weaker features have more crystalline contribution. We show that this correlation is also valid to disks around low-mass stars as well as for brown

---

[1] Steward Observatory, University of Arizona, 933 North Cherry Avenue, Tucson, AZ 85721, USA. [2] NASA Astrobiology Institute, NASA Ames Research Center, Moffett Field, CA 94035, USA. [3] Max Planck Institute for Astronomy, Königstuhl 17, Heidelberg, D-69117, Germany. [4] Osservatorio Astrofisico di Arcetri, Istituto Nazionale di Astrofisica, Largo E. Fermi 5, I-50125 Firenze, Italy.

*These authors contributed equally to this work.
†To whom correspondence should be addressed. E-mail: apai@as.arizona.edu